INTERFACE

Author for correspondence:
Kenta Ishimoto
e-mail: ishimoto@kurims.kyoto-u.ac.jp

THE ROYAL SOCIETY
PUBLISHING

Fluid flow and sperm guidance: a simulation study of hydrodynamic sperm rheotaxis

Kenta Ishimoto[1,2] and Eamonn A. Gaffney[3]

[1]The Hakubi Center for Advanced Research, Kyoto University, Kyoto, 606-8501, Japan
[2]Research Institute for Mathematical Sciences, Kyoto University, Kyoto, 606-8502, Japan
[3]Wolfson Centre for Mathematical Biology, Mathematical Institute, University of Oxford, Oxford OX2 6GG, UK

How does a sperm find its way? The study of guidance cues has fascinated sperm biologists and in particular the prospect of rheotaxis, that is a fluid flow orienting the direction of sperm swimming, has been the subject of extensive recent study, as readily motivated by the prospect that such guidance may be active in the mammalian female reproductive tract. For instance, it has been hypothesized that helical sperm flagellar beating is necessary for such guidance, whereas there is an extensive diversity of flagellar beating patterns, with planar sperm beating readily observed in human cells for example. In particular, such cells will not be guided by fluid flow according to hypothesized mechanisms for rheotaxis presented thus far. Here, using simulation methods, we investigate rheotaxis for a wide range of flagellar beat patterns. Providing the virtual sperm firstly does not possess a tightly circling trajectory in the absence of a background flow and secondly, remains within a region of low shear to prevent being washed away by the background flow, rheotaxis is generally observed with the sperm swimming into the flow together with a possible transverse velocity. Tight circling sperm motility, as observed in select hyperactivated sperm and CatSper mutants, is predicted to disrupt the rheotactic response, whereas confinement to low shear regions generally requires boundary accumulation, thus introducing subtleties in the relationship between rheotactic behaviours and the flagellar waveform and sperm characteristics. Nonetheless, such predictions suggest such rheotactic guidance may be more common and robust than previously thought, and we document simple criteria for the presence of rheotaxis that are consistent with our simulations and understanding, as well as reported observations to date.

1. Introduction

A fundamental question concerning spermatozoan dynamics is guidance: how does a sperm know where to go, or indeed, does it, or is it merely a case that so many sperm are released that random motility is nonetheless sufficient. However, following insemination in humans, the observed presence at any given time of only 10–1000 sperm within the expanse of the fallopian tubes suggest randomness alone is implausible in bringing the sperm to the egg at this point [1], whereas highly directed motility is also recorded in video-microscopy of sperm motility in the bovine female reproductive tract [2]. Furthermore, marine external fertilizers such as sea urchin sperm exhibit an extensive chemotactic response [3], which is reported to improve the chances of reproductive success [4] and is reviewed by Alvarez *et al.* [5].

Such observations of sea urchin sperm have previously generated the hypothesis that chemotaxis is also important for mammals [6] and a further suggested mammalian sperm guidance mechanism is thermotaxis [7], which is based on very small temperature differences along the mammalian reproductive tract. More generally, there are extensive reports of chemotactic and thermotactic response [6,7], as reviewed in a recent monograph [8], highlighting the possibility that these mechanisms may be active in mammalian

reproduction. However, in contrast, the specific role of chemotaxis and thermotaxis is reported as not established for mammals, and there are conflicting reports of mammalian spermatozoan response to thermal gradients [9]. Furthermore, both mammalian chemotaxis and thermotaxis require the maintenance of a detectable, robust, signal throughout substantial regions of the female reproductive tract for long range guidance. Thus, the prospective disruption of gradients owing to peristalsis and ciliary flows has led to the consequent suggestion that long range biochemical cues are not stable *in situ* [10], with analogous reasoning immediately relevant for thermotactic gradients.

In addition to the above explorations of prospective chemotactic and thermotactic guidance for mammalian sperm, the presence of directed flows in the female reproductive tract, such as the ciliary flows in the video-microscopy of Kölle *et al.* [2], has also generated the hypothesis that rheotaxis, i.e. the bias of sperm swimming by the direction of fluid flow, may provide a guidance cue [9]. Rheotaxis, with sperm directed to swim into the current, was first reported over a century ago [11] and many times in past decades [12–14], though more recent studies have documented the rheotactic response for a variety of sperm in further detail, as well as emphasizing its prospective importance in the female mammalian reproductive tract. For instance, it has been observed that sea urchin sperm are not biased by fluid flow, nor are CatSper mutant sperm, which possess defective calcium signal transduction, while normal motile uncapacitated mouse sperm undergo rheotaxis, as do headless sperm [9]. Further independent observations of uncapacitated normal human and bull sperm rheotaxis [10] are also reported, in studies which additionally emphasize that velocity components transverse to the flow profiles can occur.

Summarizing their observations led Miki & Clapham [9] to the hypothesis that sperm rheotaxis requires shear flow, boundary accumulation and a three-dimensional helicoid beat pattern that is also associated with sperm rolling [9]. Kantsler *et al.* [10] also distinguished helicoid flagellar waveforms for the observed boundary accumulation in their study and constructed a minimal model for the boundary accumulating rheotactic response. This formulation was based on the reorientation of a tilted conical helix, representing the flagellum in shear flow, via an asymptotic limit of a resistive force theory calculation. In addition, the sperm head was hardwired to remain near the boundary, and to swim in a straight line on average, and the no-slip conditions were not enforced on the boundary.

Under such conditions, the model will always predict rheotaxis, as the tilted conical helix always aligns its major axis with flow and analogous deductions of rheotaxis in the framework would hold for the planar rigid filament formed by projecting the conical helix onto a plane containing the cone's axis of symmetry (set the chirality parameter $\chi = 0$ in equation (41) within Kantsler *et al.*'s supplementary information [10]).

However, boundary accumulation is hardwired in such modelling predictions yet, physically, this is a subtle effect [15–17] with detailed features, such as sensitivity to flagellar wavenumber or the onset of hyperactivation, that are difficult to reconcile within simplified theories [18] and beyond the intended scope of Kantsler *et al.*'s modelling framework [10]. More generally, it is not physically clear when and if boundary accumulation can be disrupted by background flow especially for changes in the flagellar beat pattern, and thus the extent to

which sperm guidance based on rheotaxis in the vicinity of a surface is contingent on the flagellar waveform. Furthermore, the characteristics of the boundary accumulating, rheotactic sperm considered in both Miki & Clapham [9] and Kantsler *et al.* [10] correspond to one suggested modality of boundary accumulation with elliptic helicoid flagellar beating [16,19], whereas a further modality of boundary accumulation, with planar beating and straight swimming is also regularly observed in more viscous media both for human [20] and rat [19] sperm. According to Miki and Clapham's hypotheses [9], sperm under these circumstances will not rheotax, with the prospective implication that the rheotactic response may differ substantially among species and/or according to detailed conditions. However, a physical representation of sperm swimming with the ingredients required to assess the presence or absence of boundary accumulating rheotaxis has not yet been explored, even in modelling studies.

Consequently, our first objective is to use hydrodynamic numerical simulation in an investigation of boundary accumulating sperm rheotaxis, resolving the geometrical complexity of the flagellar waveform and the impact of the surface. This will allow the consideration of numerous questions, such as testing whether the mechanism presented by Miki & Clapham [9] generates rheotaxis and whether such dynamics requires an elliptical helicoid beat or whether planar flagellar waveforms can also feasibly induce rheotaxis. This additional modelling resolution will also enable the further objectives of considering whether the absence of rheotaxis in sea urchin sperm and mammalian CatSper mutants can be explained in the context of physics, rather than a detailed systems biological response, as well as briefly considering the impact of hyperactivation on the prospects of sperm rheotaxis.

2. The virtual sperm and its numerical simulation

Throughout the specification of a virtual sperm and the fluid dynamical equations, we use $\boldsymbol{\xi}$ to denote right-handed Cartesian coordinates fixed in a sperm flagellum reference frame, whose origin is located at the proximal end of the flagellum, with an associated orthonormal basis $\{\boldsymbol{e}_{\xi_i}\}$, $i \in \{1, 2, 3\}$. In addition, we define $\boldsymbol{x} = (x_1, x_2, x_3) := (x, y, z)$ to be Cartesian coordinates fixed in the inertial reference frame of the laboratory, with orthonormal basis $\{\boldsymbol{e}_i\}$, $i \in \{1, 2, 3\}$.

2.1. The virtual sperm flagellum

Given the importance attached to an elliptical helicoid waveform in recent experimental studies of rheotaxis [9,10], we focus on this beat pattern, initially with a conical envelope which is symmetric around the ξ_3 axis, as illustrated in figure 1*a*. The waveform is specified in the flagellar reference frame, $\boldsymbol{\xi}$, with a propagating wave, of wavenumber k and angular frequency ω, parametrized by time, t and arclength, $s \in [0, L]$, where L is the flagellum length. Thus, we have $\boldsymbol{\xi}(s, t) = (\xi_1(\xi_3), \xi_2(\xi_3), \xi_3) = (-\alpha B \mathcal{C}, B \mathcal{C}, \xi_3)$, where α corresponds to the chirality of the wave, with $\alpha = 0$ constituting a planar waveform, $\alpha > 0$ a right-handed helix as found in mouse sperm [19] and $\alpha < 0$ gives a left-handed helix, as observed for human sperm with
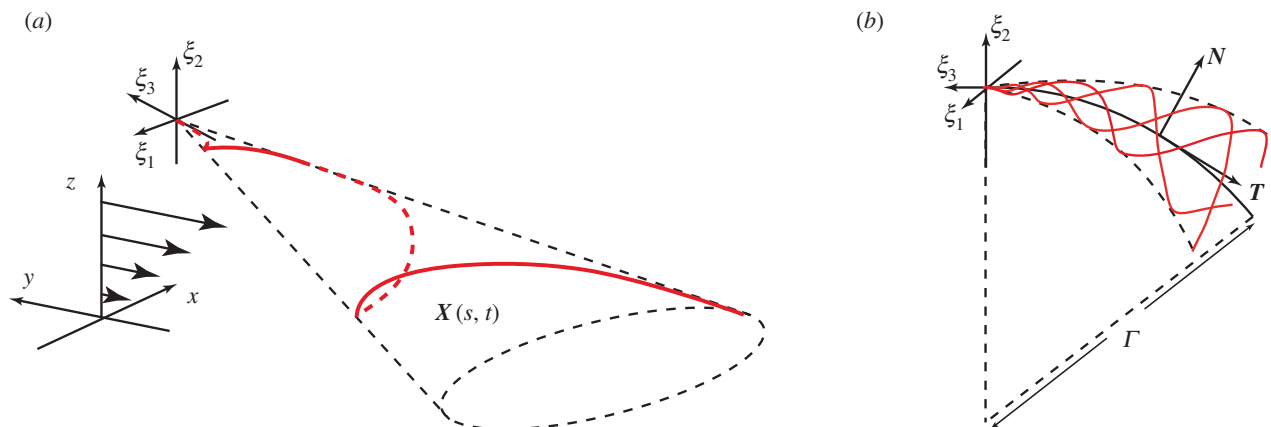
Figure 1. Reference frames and flagellar waveforms. A schematic illustrating the flagellar waveforms together with the reference frames. (*a*) The flagellar reference frame, which is right-handed, and a typical symmetric elliptical helicoid flagellar profile, as depicted in red, with $X(s, t)$ denoting the position in the laboratory reference frame for the location at time t and arclength s along the flagellum from the origin of the flagellar reference frame, $\boldsymbol{\xi} = 0$. The background shear flow is also depicted relative to the laboratory reference frame, x. (*b*) The asymmetric flagellar waveform. The centreline of a curvilinear elliptical cone is the arc of a circle of radius Γ, with unit tangent T, unit normal N and, not depicted, unit binormal $B = T \wedge N$. The flagellar wave forms a helix on this cone at any snapshot of time, with the flagellum at three different snapshots of time illustrated in red. For both (*a*) and (*b*), the time evolution of the flagellum profile corresponds to a wave propagating on the cone, away from the origin of the flagellum reference frame, $\boldsymbol{\xi} = 0$. (Online version in colour.)

$\alpha = -0.2$ [21,22]. Furthermore, B is a measure of the waveform amplitude, $\mathcal{C} := \cos(k\xi_3 - \omega t)$ and

$$s(\xi_3) = \int_{\xi_3}^{0} d\hat{\xi}_3 \left[1 + \left\{ \frac{d\xi_1}{d\hat{\xi}_3}(\hat{\xi}_3) \right\}^2 + \left\{ \frac{d\xi_2}{d\hat{\xi}_3}(\hat{\xi}_3) \right\}^2 \right]^{1/2}, \quad (2.1)$$

takes values in $[0, L]$, as depicted in figure 1.

To generate asymmetric waveforms, the axis of symmetry of the enveloping cone of the elliptical helicoid is mapped onto a segment of a circle of radius Γ, given by $(\Gamma - \xi_2)^2 + (\xi_3)^2 = \Gamma^2$, with an orientation given by the direction of decreasing ξ_3, as shown by the centreline in figure 1*b*. Let $\bar{\xi}_3$ denote the third flagellar reference frame coordinate along this curve, with $\bar{\xi}_1$, $\bar{\xi}_2$ normal and binormal coordinates, and let T, N, B denote the tangent, normal and binormal unit vectors. Then, the asymmetric waveform is given by

$$\boldsymbol{\xi}(s, t) = \bar{\xi}_1(\bar{\xi}_3)\mathbf{N}(\bar{\xi}_3) + \bar{\xi}_2(\bar{\xi}_3)\mathbf{B}(\bar{\xi}_3) + \int_{\bar{\xi}_3}^{0} d\hat{\xi}_3\, \mathbf{T}(\hat{\xi}_3)$$

$$= [-\alpha B\mathcal{C}]\mathbf{N}(\bar{\xi}_3) + [B\mathcal{C}]\mathbf{B}(\bar{\xi}_3) + \int_{\bar{\xi}_3}^{0} d\hat{\xi}_3\, \mathbf{T}(\hat{\xi}_3) \quad (2.2)$$

and

$$s(\bar{\xi}_3) = \int_{\bar{\xi}_3}^{0} d\hat{\xi}_3 \left[1 + \left\{ \frac{d\bar{\xi}_1}{d\hat{\xi}_3}(\hat{\xi}_3) \right\}^2 + \left\{ \frac{d\bar{\xi}_2}{d\hat{\xi}_3}(\hat{\xi}_3) \right\}^2 \right]^{1/2}, \quad (2.3)$$

where $\mathcal{C} := \cos(k\bar{\xi}_3 - \omega t)$ and $s \in [0, L]$.

We denote the position of the flagellum at time t and arclength s relative to the laboratory frame by $X(s, t)$, which is given by mapping $\boldsymbol{\xi}(s, t)$ from the flagellum reference frame to the laboratory. Initially, the sperm is located at $X(s = 0, t = 0) = (0,0,0.1L)$ and its orientation is such that e_{ξ_3} is in the x–z plane pointing in the direction of increasing x (see the electronic supplementary material for a demonstration that the initial orientation in the x–y plane does not alter the final dynamics). Finally, the initial acute angle of attack between e_1 and e_{ξ_3}, that is $\theta_{\text{init}} := \cos^{-1}(e_1 \cdot e_{\xi_3})$, is given by either (i) $\theta_{\text{init}} = 0$ or (ii) $\theta_{\text{init}} = 0.2\pi$.

2.2. The virtual sperm head: a modelling estimate in justifying its neglect

For sperm, the head is relatively small compared with the lengthscale of the flagellum and so in §2 of the electronic supplementary material, we consider the errors associated with neglecting the head in calculating sperm trajectories, especially their curvature and thus the impact of rheotactic guidance cues. We demonstrate that classical calculations reveal a neglect of the sperm head induces relative errors of about 20% in the swimming speed, whereas the torques owing to a sperm head are about three orders of magnitude smaller than those owing to the flagellum, and hence head torques are negligible.

Hence, neglecting the sperm head entails that angular velocities are generally accurate and linear velocities are of the correct scale; furthermore, the predicted linear velocities are *overestimates* as the head increases drag. This entails that the sperm is predicted to swim further for a given change in its orientation and hence its trajectory curvature is underestimated. In this paper, the sperm head is neglected and thus rheotactic effects are marginally *underestimated*, though the qualitative details are correct, as confirmed by the observation that headless spermatozoa rheotax in the same manner as cells with standard morphologies [9]. Finally, we note that further modelling uncertainties entail that the increased computational complexity of including head corrections would be poorly motivated, as detailed further below.

2.3. Determining the sperm trajectory and the possibility of a rheotactic response

We have the location of the flagellum relative to the flagellum reference frame, which moves at an *a priori* unknown velocity, U, and angular velocity, Ω, relative to the laboratory frame. Taking into account the presence of a no-slip surface, located at $x_3 = 0$ and a half-space domain $x_3 \geq 0$, or other boundary conditions as appropriate, we proceed to overview how low Reynolds number fluid dynamics can determine U, Ω. These can then be integrated to construct the sperm trajectory and

rheotaxis is predicted if the trajectory associated with the sperm turns into, or away from, the direction of a background flow.

2.3.1. The flow field and the background flow field

Let $p(\boldsymbol{x})$, $\boldsymbol{u}(\boldsymbol{x})$ denote the pressure and velocity field, with $p^{\infty}(\boldsymbol{x})$, $\boldsymbol{u}^{\infty}(\boldsymbol{x})$ the pressure and velocity associated with the background flow, assumed throughout this study to be the solution of Stokes' equation for a linear shear flow

$$p^{\infty}(\boldsymbol{x}) = 0, \quad \boldsymbol{u}^{\infty}(\boldsymbol{x}) = -\dot{\gamma}x_3\mathbf{e}_2, \quad (2.4)$$

with $\dot{\gamma} = 0.1T^{-1}$, where T is the sperm flagellum beat period.

2.3.2. The surface potential

We also assume a repulsion potential at very close distances to $z = 0$ to prevent the sperm crashing into this boundary, which is generally a no-slip solid surface in this study, though other boundary conditions are considered, particularly to ascertain the influence of the boundary on sperm dynamics.

Surface repulsion potentials are observed on bringing cells close to a surface, on the scale of tens to 100 nm, but the quantitative details depend on the cell, the surface and the physiological solutes [23]. In effect, we are assuming that the sperm is repelled from the surface at molecular scales, as achieved for human sperm experiments with glassware using dilute human serum albumin [20]. As motivated in the electronic supplementary material, a simple repulsive potential is used [24], and the body force per unit length of the flagellum is given by

$$\boldsymbol{f}^{\text{rep}} = g\frac{\mathrm{e}^{-x_3/d}}{1 - \mathrm{e}^{-x_3/d}}\mathbf{e}_3 = \nabla\psi^{\text{rep}},$$
$$\psi^{\text{rep}} = gd\ln(1 - \mathrm{e}^{-x_3/d}), \quad (2.5)$$

with $g = 10\,\mu LT^{-1}$ a measure of the overall repulsion, where μ is the fluid viscosity. The parameter $d = 0.005\,L = 280$ nm is a measure of the repulsion potential decay length, which is larger than the scale of 50 nm observed for bacteria [23], but details this close to the surface are qualitative only as the surface potential varies with cell, solute and surface and is not documented for sperm.

The impact of variation in d on the quantitative details of trajectory curvatures is briefly presented in §3 of the electronic supplementary material where it can be seen that d influences trajectory curvatures, though not the qualitative details and not to the extent that d can be inferred from sperm observations. Thus, the surface potential represents a source of modelling uncertainty which mitigates against the additional computational expense of including a sperm head in the modelling.

2.3.3. The prediction of sperm swimming trajectories

By linearity $p - p^{\infty}$, $\boldsymbol{u} - \boldsymbol{u}^{\infty}$ also satisfy Stokes' equations. The solution of these equations yield the instantaneous velocity, $\boldsymbol{U}$, and angular velocity $\boldsymbol{\Omega}$ of the virtual sperm at a fixed time point, given the virtual sperm is subject to the forces from the repulsive surface potential force which prohibits swimming distances closer than approximately $2d$ from the surface at $z = 0$.

This is detailed in §3 of the electronic supplementary material, where the numerical algorithm, the regularized Stokeslet method [25,26], is described and validated in depth. One must note that the solutions differ significantly according to the boundary conditions imposed at $z = 0$, with the imposition of no-slip referred to as the Blakelet solution, because

the Regularized Stokeslet method uses solutions to Stokes' equations known as Blakelets [27] in the numerical procedures. For analogous reasons, the solutions associated with a fixed tangential stress, matching that of the background shear flow, and no normal velocity at $z = 0$ are referred to as Imagelet solutions [28], and the solutions with no constraints at $z = 0$ are referred to as Stokeslet solutions [29]. Note that the imposition of a fixed tangential stress and zero normal velocity at $z = 0$ corresponding to the Imagelet solutions, may not be relevant in most physical situations, and similarly for the Stokeslet solution given the surface repulsion potential force is retained. Nonetheless, these solutions are extremely informative in assessing the extent to which hydrodynamic interactions between the surface and the cell influence the rheotactic response in interpreting the results below.

Finally, once one can determine the instantaneous velocity, $\boldsymbol{U}$, and angular velocity $\boldsymbol{\Omega}$ of the sperm cell, its position is updated—iterating, the virtual sperm swimming trajectory can be constructed, again as detailed and validated in §3 of the electronic supplementary material.

In turn, these numerical predictions will allow the exploration of the propensity for a virtual sperm to rheotax, that is for the sperm to possess a swimming trajectory whose direction is biased by the presence of a background flow. It will also enable a study of how rheotactic behaviour is related to boundary accumulation, i.e. swimming indefinitely in a region of low shear near the interface at $z = 0$, which characterizes the origin of the repulsive surface potential used throughout this study and typically, but not always, is modelled as a no-slip surface.

3. Results

In all the presented results below the mass, length and time units are such that the non-dimensional viscosity, flagellum length and frequency are of unit value.

3.1. Elliptical helicoid beating in shear flow near and distant from surfaces

We first of all consider the effects of shear for a virtual sperm with the same flagellar chirality as human sperm, which is of opposite parity to that of mouse sperm. Hence, the flagellar parameters are given by table 1 with the waveform parameters $\alpha = -0.2$, $\Gamma = \infty$, with the latter imposed to ensure a symmetric beat pattern, as specified by equation (2.1). The shear flow is given by equations (2.4) and (2.5), with parameters as in table 2.

The Blakelet solution for a no-slip surface at $x_3 \equiv z = 0$ exhibits boundary accumulation and rheotaxis, whereby the virtual sperm swims into the flow, as observed in figure 2. There is also a transverse velocity, in the same direction as the predictions and observations of Kantsler et al. [10]. Furthermore, the direction of the transverse velocity changes with chirality parity, as seen in figure 2, and this switch is also observed in the presence of a flat surface with specified tangential stress, corresponding to the Imagelet solution.

In figure 2, projected trajectories are also presented for the Stokeslet solution, which corresponds to the absence of hydrodynamic surface interactions from the boundary conditions on the flat plane. The repulsive surface potential, equation (2.5), which is due to many factors such as van
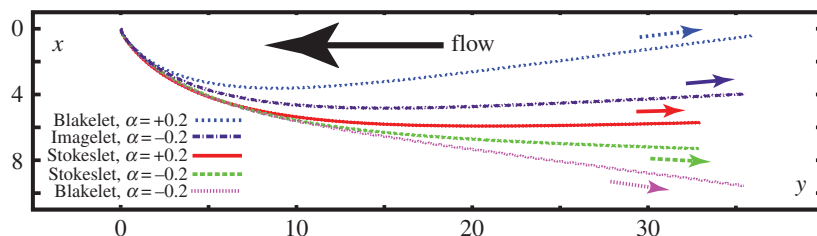
Figure 2. The effect of shear on computed sperm trajectories in a background flow with a surface repulsion potential, specified by the parameters of table 2. The virtual sperm has a symmetric flagellar envelope, $\Gamma = \infty$, with $\alpha = -0.2$, corresponding to human sperm chirality, or $\alpha = +0.2$, corresponding to the opposite chirality found in mouse, while the initial attack angle is $\theta_{init} = 0.2\pi$ and the sperm is initially located at $X(s = 0, t = 0) = (0, 0, 0.1)$. Other parameters are given in table 1. Given the initial conditions, we are observing virtual sperm behaviour in the vicinity of the origin of the repulsive surface potential at $z = 0$ and the trajectories are presented in terms of their projection onto the $x-y$ plane, thus representing paths that would be observed in the focal plane of a microscope when viewed from above. The trajectory labelled *Blakelet* gives the predicted path of this sperm near a no-slip surface, whereas the trajectory labelled *Imagelet* is the prediction for this sperm near a surface of fixed tangential stress and no normal velocity. The predictions for the *Stokeslet* correspond to the absence of hydrodynamic wall effects, though the surface repulsion potential is still included in the model. (Online version in colour.)

Table 1. Reference parameter values for the flagellum waveform, with details on the motivation for the parameter estimates presented in §1 of the electronic supplementary material.

parameter	interpretation	value
L	flagellar length	56 μm
$1/T = \omega/[2\pi]$	beat frequency	14 Hz
α	chirality parameter	$\pm \{0, 0.01, 0.05, 0.1, 0.2\}$
Γ/L	asymmetric waveform parameter	$\{0.5, \infty\}$
kL	wavenumber	3π
B	flagellar envelope parameter	$0.2\,L$
a	flagellar radius	$0.01\,L$

Table 2. Reference parameter values for the shear flow and the surface repulsion potential, noting that μ is the fluid viscosity with details on the motivation for the parameter estimates in §1 of the supplementary material.

| parameter	interpretation	value
$\dot{\gamma}$	background shear flow strength	$0.1\,T^{-1}$
g/μ	repulsion potential magnitude	$10\,LT^{-1}$
d	repulsion potential lengthscale	$0.005\,L$

der Waals forces but *not* hydrodynamics, is taken into consideration and, owing to the cell rotation arising from the elliptical helicoid beat pattern, the virtual sperm oscillates in and out of the region of influence of this potential (as also observed in figure 3b), confining it to a region of low shear flow. Rheotaxis in the $x-y$ plane is also observed, emphasizing that a surface hydrodynamic interaction is not required for rheotaxis, as described in Kantsler *et al.*'s minimal model, though restriction to regions of sufficiently low flow is required.

Furthermore, in figure 3, we consider further simulations of the virtual sperm with $\alpha = -0.2$, corresponding to the chirality of human sperm, but now with variation in the initial distance from the no-slip surface, denoted h. We see that once this initial distance reaches 20% of the flagellum length, $h = 0.2$ which is about 11 μm for human sperm,

boundary accumulation is lost, and the sperm is swept downstream without a discernible rheotaxis as it enters the bulk, faster, flow with increasing z. Hence, we see that constraining the sperm to remain in a low flow region is an important feature of rheotaxis and this can be achieved by boundary accumulation.

3.2. Planar beating in shear flow near a no-slip surface

We proceed to consider sperm swimming in a shear flow near a no-slip surface at $x_3 \equiv z = 0$ with a planar flagellar beat. We have a virtual human sperm with a symmetric flagellar waveform given by equation (2.1), using the parameters of table 1 with a flagellar length $L = 56$ μm and waveform parameters $\alpha = 0$, $\Gamma = \infty$. In particular, $\alpha = 0$ ensures the flagellar waveform is the projection of an elliptical helicoid beat onto the plane containing its axis of symmetry. The shear flow and repulsion forces are given by equations (2.4) and (2.5), respectively, with the parameters specified in table 2. In figure 4a, one can observe that this planar beating virtual sperm also rheotaxes into the direction of the flow, and thus chirality is not necessary for rheotaxis. Furthermore, the planar beater trajectory has no transverse velocity for asymptotically long time and also possesses a larger radius of curvature at intermediate times, consistent with observations that the trajectories of sperm with nearly planar beats have reduced curvature [10]. From figure 4b, we also predict that the simulated virtual sperm boundary accumulates very close to the no-slip surface, at a height of
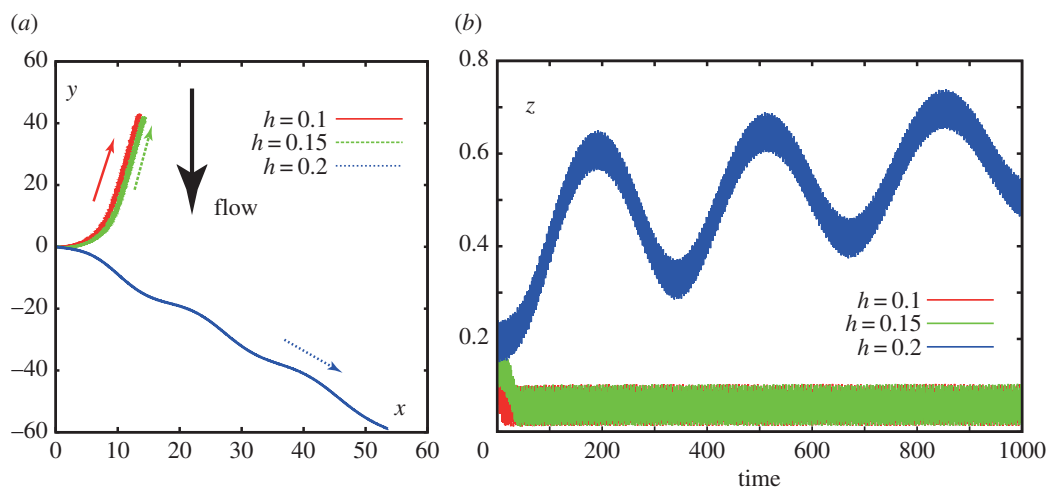
Figure 3. The influence of the surface on computed sperm trajectories in a background flow and surface repulsion potential, specified by the parameters of table 2. (a) A virtual sperm in the presence of a no-slip surface is considered with sperm parameters values given in table 1 and also that $\Gamma = \infty$, $\alpha = -0.2$, $\theta_{init} = 0$, $X(s = 0, t = 0) = (0, 0, h)$. The projection of the trajectory onto the plane of the no-slip surface is plotted for this sperm with the arrow showing the direction of swimming for different non-dimensional starting heights, h, above the no-slip surface. (b) A further breakdown of this virtual sperm's trajectory, with plots of z, its distance from the no-slip surface, as a function of time for different starting heights above the no-slip surface. (Online version in colour.)
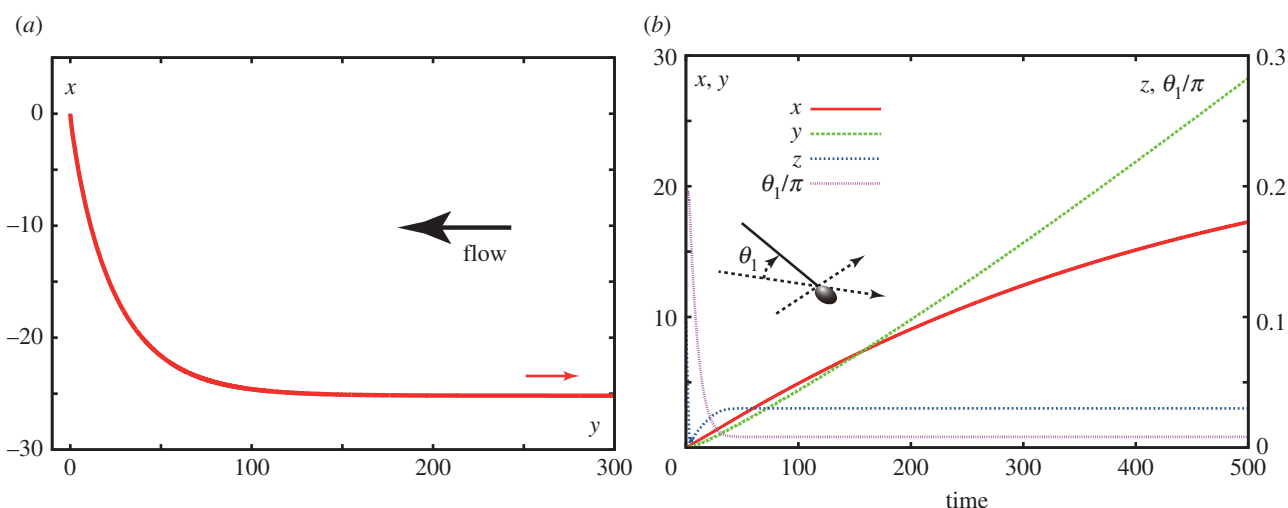
Figure 4. Planar swimming sperm dynamics in a background flow and surface repulsion potential, specified by the parameters of table 2. (a) A virtual sperm in the presence of a no-slip surface is considered with sperm parameter values of table 1, and the further specification with $\Gamma = \infty$, $\alpha = 0$, $\theta_{init} = 0.2\pi$ and the sperm is initially located at $X(s = 0, t = 0) = (0, 0, 0.1)$. The projection of the trajectory onto the plane of the no-slip surface is plotted for this sperm with the smaller arrow showing the direction of swimming. (b) A further breakdown of this virtual sperm's trajectory, with plots of x, y, z as a function of time together with θ_1, its angle of attack relative to the no-slip surface, that is the angle between the ξ_3 axis and the no slip surface $z = 0$. The sperm head in the figure is solely for illustration of the definition of the angle and has not been considered in the modelling. (Online version in colour.)

$\approx 0.03L$ approximately 7 μm, with a tiny angle of attack, so that the possession of a flagellum elevated into the shear flow, as with elliptical helicoid beaters, is again not a necessary feature of rheotaxis.

3.3. Asymmetric flagellar beating in shear flow near a no-slip surface

Finally, we explore the impact of flagellar waveform asymmetry on rheotaxis in shear flows with a no slip boundary at $x_3 \equiv z = 0$. We consider a virtual sperm possessing an asymmetric flagellar waveform, given by equation (2.2) with the chirality parameter α specified in figure 5 and the radius of curvature of the flagellar waveform, Γ, is equal to 0.5. The shear flow and repulsion forces are those used previously and given by equations (2.4) and (2.5), respectively, with the parameters of table 2, except for trajectories in the absence of shear, for

which the shear strength, $\dot{\gamma}$, is zero. In figure 5a, the trajectories associated with asymmetric waveform swimmers are projected onto the no-slip plane, whereas a side view of these trajectories is presented in figure 5b.

In the absence of shear and chirality, the virtual sperm has a planar asymmetric wave associated with a sea urchin beat pattern. In figure 5a,b, its trajectory is presented in red, and one can observe that this sperm boundary accumulates and executes tight swimming circles with a diameter on the scale of a cell length, consistent with observations which range from 25 [30] to roughly 100 μm [9], depending on experimental details. On introducing a shear flow, the resulting trajectory is plotted in green; one can observe that boundary accumulation is not disrupted, even if the transients are different, and that the swimming turning circles persist, though the sperm is slowly swept downstream at a rate of about 0.02 cell lengths per beat cycle.
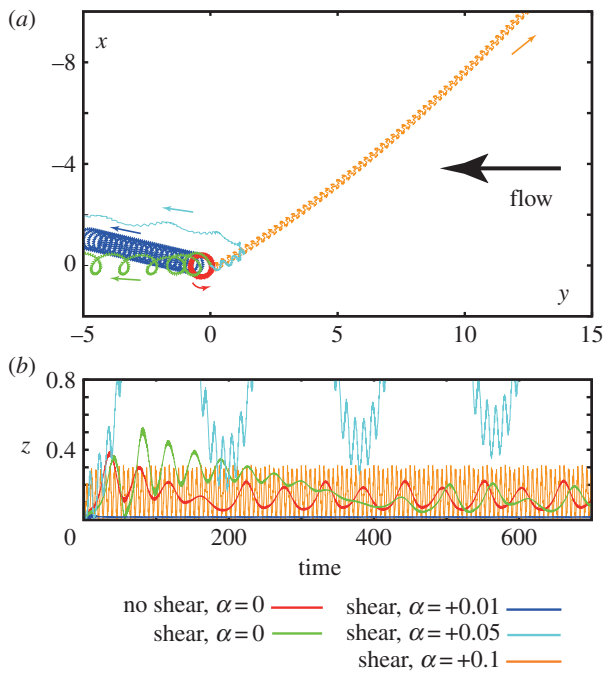
Figure 5. The impact of an asymmetric flagellar waveform for a sperm swimming in a background flow and surface repulsion potential, specified by the parameters of table 2, with a no-slip surface at $z = 0$. For all trajectories, the parameters are given by table 1 with α as specified, $\Gamma = 0.5$, $\theta_{init} = 0.2\pi$ and the initial location $X(s = 0, t = 0) = (0, 0, 0.1)$. The exception is the red trajectory, which circles around the same spot in plot (a), and corresponds to no background flow. (a) The projection of the trajectories onto the plane of the no-slip surface. (b) Time course of the height z of the flagellum above the surface, as measured from the origin of the flagellar frame. (Online version in colour.)

Introducing a small chirality, with $\alpha = +0.01$ for the navy trajectory in figure 5, induces no substantial effect; the virtual sperm still boundary accumulates, albeit *much* closer to the surface, with $z \approx 0.02$, and executes turning circles with a slow downstream drift of about ≈ 0.005 cell lengths per beat cycle, owing to the smaller shear velocity at the boundary accumulation height. A small, chirality-induced, transverse drift velocity to the flow is predicted and, as detailed in §4 of the electronic supplementary material, once non-trivial flagellar chirality is present the direction of rotation near the no-slip surface is dictated by the sign of the chirality via boundary accumulating behaviours.

These predictions are consistent with observations of many marine sperm, such as sea urchin and *Ciona*, which exhibit circling trajectories with a single rotation direction [9,19,31], determined by the sign of the flagellar chirality [32] which is anticlockwise when viewed from above for a positive chirality [19]. Furthermore, while the predicted slow downstream drift is not explicitly observed in the shear flow experiments of Miki & Clapham [9] such effects would be difficult to discern in the duration of these experiments as, for example, the sperm execute less than a single revolution and the magnitude such effects would also be contingent on the quantitative details, such as the boundary accumulation height.

With further increases in chirality, with $\alpha = +0.05$ as depicted in cyan in figure 5, boundary accumulation is lost and the virtual sperm is swept downstream. This emphasizes how the presence or absence of rheotaxis near a surface inherits a subtle dependence on the waveform, associated

with the presence or absence of boundary accumulation. Finally, as reported in §4 of the electronic supplementary material larger magnitudes of chirality induce a relatively progressive sperm motility. Such a virtual sperm does not exhibit a highly curved path in the absence of flow and, when subjected to shear flow, rheotaxis is predicted to occur once boundary accumulation is also present, as illustrated in figure 5 for $\alpha = 0.1$.

More generally, these observations of virtual sperm emphasize that rheotaxis requires sperm to persist in regions of relatively low shear, so that they are not swept away, and the predictions for the absence of rheotaxis in sperm with highly asymmetric flagellar waveforms is consistent with simply whether the flagellar asymmetry induces an angular velocity that dominates rheotactic-induced turning, or vice versa.

4. Discussion and conclusions

We have theoretically considered sperm swimming in a background shear flow to explore the prospects for rheotaxis, the directed bias of sperm swimming by the flow together with the potential requirements for this guidance cue to be observed, using an elliptical helicoid flagellar beating given that recent experimental studies have focused on this beat pattern [9,10]. In our validation studies in the absence of a background flow, as presented in the electronic supplementary material, we have observed that sperm with this beat pattern typically boundary accumulate with a significant trajectory curvature for the beat-period averaged path near a no-slip surface. In particular, this mode of boundary accumulation differs from the hydrodynamic boundary capture theoretically explored in [17,28] and much of [16], where the repulsive surface potential was not taken into consideration. Thus, we often work in the regime where the virtual cell reaches far closer to the surface, so that shear does not wash the cell downstream, and hence the accumulation heights in this study, which generally satisfy $h < 0.05L$, are much smaller than that predicted by simply the hydrodynamic interaction of the cell and the boundary, in the absence of a surface repulsion potential.

The trajectory curvature of the boundary accumulated cell can be readily understood. For an elliptical helicoidal beat pattern, there is greater viscous drag on the flagellum nearer a no-slip surface in total, over a whole beat cycle, generating a net viscous torque about the z-axis. As the cell must be torque-free, this drag is compensated by the torques induced by an angular velocity of the cell about the z-axis; hence, the trajectory curves in the x–y plane. In contrast, the planar swimmer near a surface will possess a very small angle of attack as seen in figure 4b, and previous work [16,17], and thus this effect will be negligible, leading to effectively no trajectory curvature as seen in simulations [16,17] and experiments [20]. Furthermore, in the presence of a flat surface with a fixed tangential stress, which is zero if there is no background shear flow, there is less viscous drag for motion parallel to the boundary, and thus, the trajectory curvature is in the opposite direction, as confirmed both theoretically and experimentally for bacteria [33], which also swim with rotation. Similarly, by this mechanism, one has that changing the chirality parity of the flagellar wave changes the directions of the torques, and thus, the direction of the surface induced trajectory curvature.

In the presence of shear flow $u^{\infty} = -\dot{\gamma}z e_2$, which is sufficiently weak to allow sperm to swim against the current if they stay within the vicinity of $z = 0$, rheotactic guidance is observed, with the virtual sperm turning into the flow, which is compatible with observations [9,10]. The fact the bias in the trajectory to turn into the flow is identical both near a no-slip surface and a flat surface of fixed tangential stress rules out a trajectory curvature via surface interaction torques and also shows that the latter is negligible compared with torques induced by rheotaxis for a sperm that is not aligned with the background flow. Nonetheless, the predicted transverse velocity is of the opposite sign on comparing a flat, tangential stress surface and a no-slip surface, indicating that this specific aspect of the rheotactic phenomenon is related to surface hydrodynamic effects. The direction of the transverse velocity, once rheotaxis into the flow has been established, is consistent with simply the superposition of surface-induced trajectory curvature with, for example, a switch in the transverse velocity direction on changing the sign of the flagellar waveform chirality. The surface trajectory curvature is not the only effect in that a smaller chiral-dependent transverse velocity is predicted to persist even for the *Stokeslet* solution in the absence of hydrodynamic surface interactions, though the virtual sperm is constrained near $z = 0$ because of the repulsive surface potential which is due to many factors, such as van der Waals forces. Thus, we predict that surface interactions dominate the transverse velocity associated with the rheotaxis of an elliptical helicoid swimmer, though chirality-dependent corrections are also present; furthermore, an analytical model rich enough to include rheotaxis, and the contrasting influence of different surfaces and chirality in particular requires an extension of existing modelling frameworks.

We also note that rheotaxis is predicted to occur even when the sperm is not in the vicinity of a surface, as long as the sperm is confined in a region where the background flow is insufficient to wash the sperm away, as implicit in Kanstler *et al.*'s minimal model [10]. In particular, the *hydrodynamic* interaction of a surface and the sperm is not required, as highlighted by the Stokeslet solutions of figure 2 where, via the surface repulsion potential, the sperm is constrained to remain in a region with sufficiently low shear flow to prevent washout. This reasoning would indicate that rheotaxis can occur in the bulk, as observed for bacteria [34], but with the simple shear flows typically considered in experimental and theoretical investigations of sperm one simply has washout, unless the sperm persists in the region of low shear close to the boundary. In particular, within confining geometries, such as microdevices or the female reproductive tract, rheotactic directed guidance in the bulk is not inconsistent with this study, as the flow does not increase indefinitely away from boundaries.

Furthermore, a virtual planar beater will rheotax without a large angle of attack into a surface, highlighting that the planar beat patterns of boundary accumulating human sperm in viscous media do not preclude rheotaxis, and more generally that rheotaxis need not be as sensitive to the flagellar waveform as suggested in earlier studies [9]. In particular, chirality and a significant angle of attack relative to a surface are not mechanically required. Nonetheless, we have also observed predictions that an asymmetric beat with tight circling is sufficient to prevent rheotaxis, consistent with observations that sea urchin and CatSper mutant sperm do not rheotax. The mechanical explanation for this is simple. A shear flow induces a torque on a swimmer unless it is already aligned with the flow, as

illustrated in Kantsler *et al.*'s minimal model [10]. If this is the dominant torque owing to the flagellar dynamics the trajectory will possess a curvature generating a compensating torque, so that the cell is torque-free as required in the inertialess limit, which induces the rheotactic response causing the swimmer to align with the flow. However, if the torques on the flagellum are dominated by another aspect of the flagellar motion, such as asymmetry, the compensating torque governing the flagellar trajectory will predominantly compensate *this* dominating feature, rather than the shear-flow-induced torque, subordinating a rheotactic response.

In summary, we have the simple prediction that rheotaxis requires (i) a confining influence to prevent sperm reaching flow rates that will sweep them away typically, but not necessarily, a boundary or a confined geometry and (ii) in the no-flow scenario, an absence of sperm circling that would subordinate the rheotactic response. This is a much weaker set of requirements than originally proposed for sperm [9] and is consistent with all modelling results presented here and previous observations, in turn suggesting that rheotaxis may be even more prevalent as a guidance mechanism.

We reconsider the planar beating sperm in view of these criteria. Let U denote its swimming speed, H denotes its boundary accumulation height and we assume this is not significantly altered by the presence of a shear flow $u^{\infty} = -\dot{\gamma}z e_2$ and also that boundary accumulation is the only means by which sperm can be constrained to low shear-flow regions. Then, the above conditions for rheotaxis near a surface are

$$\dot{\gamma} \ll \frac{U}{H}, \quad R_{\mathrm{rheo}} \ll R_{\mathrm{turn}}, \tag{4.1}$$

where R_{rheo} is the radius of curvature of the trajectory associated with the initial rheotactic response and R_{turn} is the radius of curvature associated with the shear-flow free swimming. From our simulation of a planar beater, figure 4a, we find $R_{\mathrm{rheo}} \approx 40L$; assuming the rheotactic trajectory curvature, R_{rheo}^{-1}, has a linear dependence on the shear rate, as observed in the calculations of Kantsler *et al.* [10], we have $R_{\mathrm{rheo}} \approx 4L\omega/\dot{\gamma}$, where the frequency dependence is required on the grounds of dimensional consistency. Defining a non-dimensional rheotactic number, $\mathcal{R}$ and a non-dimensional shear rate, $\mathcal{S}$, by

$$\mathcal{R} := \frac{UR_{\mathrm{turn}}}{L\omega H} \quad \text{and} \quad \mathcal{S} := \dot{\gamma}\frac{R_{\mathrm{turn}}}{\omega L} \tag{4.2}$$

we have from the conditions (4.1) the prediction that $\mathcal{R} \gg 4$ is a necessary condition for rheotaxis in that case rheotaxis will manifest on increasing shear rates once $\mathcal{S} \gg 4$.

Similarly, for the elliptical helicoid beating, with analogous assumptions, we find $\mathcal{R} \gg 1$ is a necessary condition for rheotaxis, which will occur on increasing shear rates once $\mathcal{S} \gg 1$. The non-dimensional factors that differ between the planar beater and the elliptical helicoid beat arise from inspecting the numerical predictions for R_{turn} and thus will certainly differ according to detailed beat pattern and other complexities, such as the sperm head shape; as such these conditions for rheotaxis are crude order of magnitude estimates. Nonetheless, when the rheotactic number $\mathcal{R}$ is sufficiently large it is predicted that rheotaxis can occur, at least for an appropriate choice of shear rate.

For illustration we demonstrate in §5 of the electronic supplementary material that the lack of sea urchin sperm surface rheotaxis in experiments [9] is predicted by the rheotactic

conditions; analogous deductions are presented for CatSper mutants. This analysis in the electronic supplementary material proceeds to consider the above rheotactic criteria for star-spin hyperactivated human sperm [35], which are predicted to fail to rheotax. In contrast, for the hyperactivation of mouse sperm in viscous solution, where essentially straight line swimming becomes manifest [9], the potential for sperm rheotaxis is indicated, at least given boundary accumulation, though in this experimental study it is also difficult to estimate the turning circle of these sperm for more precision. The requirement for boundary accumulation however is counter-indicated in previous simulations of hyperactivated sperm [17] though geometrical confinement may also be relevant for a rheotactic response. Nonetheless, this latter caveat also highlights that the complexities of boundary accumulation, such as a flagellum wavenumber dependence [16,17], are implicitly inherited by the criteria for boundary accumulating rheotaxis via the accumulation height, H.

In summary, we have explored the rheotactic response of virtual sperm via a detailed simulation study, using a sperm model of a prescribed planar, or ellipsoidal helical, waveform and a negligibly small sperm head. This virtual sperm typically rheotaxes in shear flow, turning into the upstream direction. In practice, boundary accumulation is required to confine the sperm to a region of sufficiently small flow so as to prevent washout, though the actual interactions between the virtual sperm and the boundary are subordinate to the rheotactic response. Nonetheless, these interactions induce a small transverse velocity perpendicular to the flow direction once rheotaxis is established for non-planar waveforms. In contrast, tightly circling swimming sperm, owing to asymmetric flagellar waveforms, do not rheotax as the torques owing to the asymmetric waveform dominate the directionality of the sperm trajectory. Hence, we have suggested that rheotaxis requires confinement, simply to prevent washout, and a sufficiently weak circling swimming trajectory in the absence of flow, with order of magnitude constraints for the realization of rheotaxis via boundary accumulating confinement. These latter constraints explain previous observations [9,10], as well as our own simulation results, suggesting that rheotaxis can readily achieve sperm guidance across many different species providing the flagellar waveform is not significantly asymmetric and the cell boundary accumulates, or otherwise remains within regions of relatively low flow.

References

1. Croxatto HB. 2002 Physiology of gamete and embryo transport through the fallopian tube. *Reprod. Biomed.* **4**, 160–169. (doi:10.1016/S1472-6483(10)61935-9)

2. Kölle S, Dubielzig S, Reese S, Wehrend A, König P, Kummer W. 2009 Ciliary transport, gamete interaction, and effects of the early embryo in the oviduct: *ex vivo* analyses using a new digital videomicroscopic system in the cow. *Biol. Reprod.* **81**, 267–274. (doi:10.1095/biolreprod.108.073874)

3. Ward GE, Brokaw CJ, Garbers DL, Vacquier VD. 1985 Chemotaxis of *Arbacia punctulata* spermatozoa to resact, a peptide from the egg jelly layer. *J. Cell Biol.* **101**, 2324–2329. (doi:10.1083/jcb.101.6.2324)

4. Zimmer RK, Riffel JA. 2011 Sperm chemotaxis, fluid shear, and the evolution of sexual reproduction. *Proc. Natl Acad. Sci. USA* **108**, 13 200–13 205. (doi:10.1073/pnas.1018666108)

5. Alvarez L, Friedrich BM, Gompper G, Kaupp UB. 2014 The computational sperm cell. *Trends Cell Biol.* **24**, 198–207. (doi:10.1016/j.tcb.2013.10.004)

6. Ralt D *et al*. 1994 Chemotaxis and chemokinesis of human spermatozoa to follicular factors. *Biol. Reprod.* **50**, 774–785. (doi:10.1095/biolreprod50.4.774)

7. Bahat A, Eisenbach M. 2006 Sperm thermotaxis. *Mol. Cell. Endocrinol.* **252**, 115–119. (doi:10.1016/j.mce.2006.03.027)

8. Cosson J (ed.). 2015 *Flagellar movement and sperm guidance*. Sharjah, UAE: Bentham Science Publishers.

9. Miki K, Clapham DE. 2013 Rheotaxis guides mammalian sperm. *Curr. Biol.* **23**, 443–452. (doi:10.1016/j.cub.2013.02.007)

10. Kantsler V, Dunkel J, Blayney M, Goldstein RE. 2014 Rheotaxis facilitates upstream navigation of mammalian sperm cells. *eLife* **3**, e02403.

11. Lott G. 1872 *Zur Anatomie und Physiologie des Cervix uteri*. Stuttgart, Germany: Ferdinand Enke.

12. Bretherton FP, Rothschild MA. 1961 Rheotaxis of spermatozoa. *Proc. R. Soc. Lond. B* **153**, 490–502. (doi:10.1098/rspb.1961.0014)

13. Roberts AM. 1970 Motion of spermatozoa in fluid streams. *Nature* **228**, 375–376. (doi:10.1038/228375a0)

14. Winet H, Bernstein GS, Head J. 1984 Observations on the response of human spermatozoa to gravity, boundaries and fluid shear. *J. Reprod. Fert.* **70**, 511–523. (doi:10.1530/jrf.0.0700511)

15. Elgeti J, Kaupp UB, Gompper G. 2010 Hydrodynamics of sperm cells near surfaces. *Biophys. J.* **99**, 1018–1026. (doi:10.1016/j.bpj.2010.05.015)

16. Smith DJ, Gaffney EA, Blake JR, Kirkman-Brown JC. 2009 Human sperm accumulation near surfaces: a simulation study. *J. Fluid Mech.* **621**, 289–320. (doi:10.1017/S0022112008004953)

17. Ishimoto K, Gaffney EA. 2014 A study of spermatozoan swimming stability near a surface. *J. Theor. Biol.* **360**, 187–199. (doi:10.1016/j.jtbi.2014.06.034)

18. Smith DJ, Blake JR. 2009 Surface accumulation of spermatozoa: a fluid dynamic phenomenon. *Math. Sci.* **34**, 74–87.

19. Woolley DM. 2003 Motility of spermatozoa at surfaces. *Reproduction* **126**, 259–270. (doi:10.1530/rep.0.1260259)

20. Smith DJ, Gaffney EA, Gadêlha H, Kapur N, Kirkman-Brown JC. 2009 Bend propagation in the flagella of migrating human sperm, and its modulation by viscosity. *Cell Motil. Cytoskel.* **66**, 220–236. (doi:10.1002/cm.20345)

21. Ishijima S, Oshio S, Mohri H. 1986 Flagellar movement of human spermatozoa. *Gamete Res.* **13**, 185–197. (doi:10.1002/mrd.1120130302)

22. Ishijima S, Hamaguchi MS, Naruse M, Ishijima SA, Hamaguchi Y. 1992 Rotational movement of a spermatozoon around its long axis. *J. Exp. Biol.* **163**, 15–31.

23. Klein JD, Clapp AR, Dickinson RB. 2003 Direct measurement of interaction forces between a single bacterium and a flat plate. *J. Colloid Interface Sci.* **261**, 379–385. (doi:10.1016/S0021-9797(03)00095-X)

24. Spagnolie SE, Lauga E. 2012 Hydrodynamics of self-propulsion near a boundary: predictions and accuracy of far-field approximations. *J. Fluid Mech.* **700**, 105–147. (doi:10.1017/jfm.2012.101)

25. Cortez R. 2001 The method of regularized Stokeslets. *SIAM J. Sci. Comput.* **23**, 1204–1225. (doi:10.1137/S106482750038146X)

26. Gillies E, Cannon RM, Green RB, Pacey AA. 2009 Hydrodynamic propulsion of human sperm. *J. Fluid Mech.* **625**, 445–474. (doi:10.1017/S0022112008005685)

27. Blake JR. 1971 A note on the image system for a Stokeslet in a no slip boundary. *Proc. Camb. Phil. Soc.* **70**, 303–310. (doi:10.1017/S0305004100 049902)

28. Ishimoto K, Gaffney EA. 2013 Squirmer dynamics near a boundary. *Phys. Rev. E* **88**, 062702. (doi:10.1103/PhysRevE.88.062702)

29. Pozrikidis C. 1992 *Boundary integral and singularity methods for linearized viscous flow*. Cambridge, UK: Cambridge University Press.

30. Woolley DM, Vernon GG. 2001 A study of helical and planar waves on sea urchin sperm flagella, with a theory of how they are generated. *J. Exp. Biol.* **204**, 1333–1345.

31. Shiba K, Baba SA, Inoue T, Yoshida M. 2008 Ca^{2+} bursts occur around a local minimal concentration of attractant and trigger sperm chemotactic response. *Proc. Natl Acad. Sci. USA* **105**, 19 312–19 317. (doi:10.1073/pnas.0808580105)

32. Ishijima S, Hamaguchi Y. 1992 Relationship between direction of rolling and yawing of golden hamster and sea urchin spermatozoa. *Cell Struct. Funct.* **17**, 319–323. (doi:10.1247/csf.17.319)

33. DiLeonardo R, Dell'Arciprete D, Angelani L, Iebba V. 2011 Swimming with an image. *Phys. Rev. Lett.* **106**, 038101. (doi:10.1103/PhysRevLett.106.038101)

34. Marcos, Fu HC, Powers TR, Stocker R. 2012 Bacterial rheotaxis. *Proc. Natl Acad. Sci. USA* **109**, 4780–4785. (doi:10.1073/pnas.1120955109)

35. Robertson L, Wolf DP, Tash JS. 1988 Temporal changes in motility parameters related to acrosomal status: identification and characterization of populations of hyperactivated human sperm. *Biol. Reprod.* **39**, 797–805. (doi:10.1095/biolreprod39.4.797)